

Supporting information

In Situ Asymmetry Engineering Constructing Superhydrophilic Hierarchical Polyacrylonitrile Nanofiber Membrane for Unprecedentedly Ultrafast Oil-Water Emulsion Separation

XiQuan Cheng,^a Zekun Sun,^a Xiaobin Yang,^{b, d} Zhixing Li,^a Yingjie Zhang,^{*a} Peng

Wang,^c Heng Liang,^c Jun Ma,^{*c} Lu Shao ^{*b}

Contents

1. Materials and methods	3
1.1 Materials	3
1.2 Characterizations	3
1.2.1 Scanning Electron Microscope (SEM) and energy-dispersive X-ray (EDX).....	3
1.2.2 Confocal Laser Scanning Microscope (CLSM)	3
1.2.3 X-ray photoelectron spectroscopy (XPS).....	3
1.2.4 Fourier infrared spectrometer (FTIR)	3
1.2.5 Contact angle measurement	4
1.2.6 Differential scanning calorimeter (DSC)	4
1.2.7 Polarized optical microscope and UV spectrophotometer	4
1.2.8 Light scattering nanometer particle size analyzer	4
2. Experimental section	4
2.1 The operation of underwater oil-adhesion	4
2.2 Oil-in-water emulsion separation.....	4
2.3 Calculation the water uptake and porosity	5
2.4 Calculation the content of non-refrigerated water.....	5
3. Results	7
3.1 ATR-FTIR spectra of membranes	7
3.2 The nanofiber diameter of PAN-H membrane.....	7
3.3 Morphology, hydrophilicity and emulsion permeances of membranes with different concentration.....	8
3.4 The cross-section morphology of PAN-PPG-AS membrane.....	9
3.5 Thickness and emulsion permeances of membranes with asymmetric structure	9
3.6 3D images of PAN-H membrane.....	11
3.7 The pore size distribution of PAN-PPG-AS membrane.....	11
3.8 Water contact angles characterization of various membranes	12
3.9 The DSC heating curve of all membranes	12
3.10 The optical microscopy characterization of emulsion.....	13
3.11 Diesel-in-H ₂ O emulsion permeance and separation efficiency	14
3.12 Nanoparticle size of emulsion and filtration	15
Notes and references.....	15

1. Materials and methods

1.1 Materials

Polyacrylonitrile (PAN) (average $M_w=150000$) was purchased from Huachuang Plasticization (Suzhou China). N-Methyl pyrrolidone ($NMP \geq 99.0\%$) was purchased from Beilian Fine Chemicals Co., Ltd. (Tianjin, China). Sodium laurylsulfonate was obtained from Guangfu Fine Chemical Research Institute (Tianjin, China). Toluene ($\geq 99.5\%$) was purchased from Far East Fine Chemical Co., Ltd. (Yantai China). Diesel was purchased from the local Sinopec gas station (Weihai China). N-octane ($>96.0\%$), poly (propylene glycol) bis (2-aminopropyl ether) (PEA Mn-400), poly (ethylene glycol) diglycidyl ether (PEGDGE Mn-500), γ -Glycidyloxypropyltrimethoxysilane (GPTMS $>97.0\%$) and Oil red O were all received from Aladding (China). Absolute ethanol was obtained from Hongsheng Fine Chemical Co., Ltd. (Changshu, China). Pure water made by the laboratory.

1.2 Characterizations

1.2.1 Scanning Electron Microscope (SEM) and energy-dispersive X-ray (EDX)

Morphologies and energy spectrum analysis of the membranes were characterized with a scanning electron microscope (SEM) and energy-dispersive X-ray (EDX) (MERLIN Compact, Zeiss Company), respectively. The uniform distribution of surface elements of the modified membrane could be observed by EDX. In addition, all samples must be pre-treated with prior spraying of gold to obtain morphology and elements distribution.

1.2.2 Confocal Laser Scanning Microscope (CLSM)

Confocal laser scanning microscope was measured to analyse the roughness of membranes by a CLSM device. 3D images of the membrane surface with RSa values can be used to characterize roughness.

1.2.3 X-ray photoelectron spectroscopy (XPS)

The chemical structure of the membrane surface was analysed X-ray photoelectron spectroscopy (XPS) using an Al $K\alpha$ X-ray source by XPS equipment (PHI-1600 X-ray photoelectron spectrometer, USA) and its derivatives under ultra-high vacuum (6×10^{-9} mbar). The source of emission was Mg $K\alpha$ and data was obtained using the SPECTRA version 8 operating system.

1.2.4 Fourier infrared spectrometer (FTIR)

Attenuated total reflectance Fourier transformed infrared spectroscopy (ATR-FTIR) was measured by FTIR equipment (Nicolet 380, Thermo Electron). It was used to analyse the chemical composition of the membranes.

1.2.5 Contact angle measurement

Water (2 μ L) contact angle and underwater oil (3 μ L) contact angle were calculated using contact angle measuring equipment (SL200B/K Kino, America). The average value of three or more measurements per sample was calculated to obtain the contact angle. The dynamic wetting and adhesion state of water droplets on the membrane surface could be accurately recorded. At the same time, the sliding angles of oil droplets (5 μ L) on the surface of the membrane could be measured in time. The sliding angle test method: determine the sine value ($\tan \theta$) by measuring the vertical height and horizontal length of the slope when the oil droplets roll.

1.2.6 Differential scanning calorimeter (DSC)

Differential scanning calorimeter equipment (DSC214, Germany) was used to characterize changes in the enthalpy of the membrane during heating. The heating rate was 10 °C/min and the temperature range was set from -80 °C to 100 °C.

1.2.7 Polarized optical microscope and UV spectrophotometer

Optical microscopy photos of emulsion before and after separation were recorded by polarized optical microscopy (BA210E, MOTIC CHINA GROUP CO., LTD.). The content of oil in water was measured by ultraviolet spectrophotometer (TU-1810, Beijing Spectrum Analysis General Instrument Co., Ltd.). The oil content of the sample was calculated by characterizing the absorbance of Oil Red O at a wavelength of 507 nm.

1.2.8 Light scattering nanometer particle size analyzer

Nanoparticle size analyzer (Zetasizer Nano ZSP, Malvern, United Kingdom) was used to analyze the size of oil droplets in emulsion before and after separation. 3 ml of sample was added to a four-sided transparent quartz cuvette for measurement.

2. Experimental section

2.1 The operation of underwater oil-adhesion

A 3 μ L oil droplet (chloroform) was used to contact and leave the membrane surface. The oil droplet was forced to contact the surface of the membrane with significant deformation and then was raised upward.

2.2 Oil-in-water emulsion separation

Firstly, 0.03 g of SLS was dissolved into 297 ml of pure water, then 3 ml of oil red O-dyed n-octane, toluene and diesel (oil red O concentration of 5 mg/100 ml) was dispersed in an aqueous solution containing a surfactant, and the whole process was continuously stirred for 10 hours or overnight. The n-octane-in-H₂O emulsion and toluene-in-H₂O emulsion were named NE and TE respectively. The oil-water separation experiment was driven by gravity (liquid level 10 ± 0.1

cm) using a laboratory-made cylindrical glass separation device (1.5 cm in diameter). The emulsion permeances were calculated using **eq.1** in the first five minutes.

$$L = \frac{V}{A \times t \times P} \quad (1)$$

where L corresponds to oil-water emulsion permeances ($L \cdot m^{-2} \cdot h^{-1} \cdot bar^{-1}$), A, t, and P correspond to the actual membrane area (m^2), operating time (h) and operating pressure (bar) respectively. The separation efficiency of all PAN membranes was calculated using **Eq.2**

$$R = \left(1 - \frac{C_p}{C_f}\right) \times 100\% \quad (2)$$

where C_p and C_f represent the solute concentrations in the permeate solution and the feed solution, respectively. Each data point is an average of three repetitions of each test, with $\pm 5\%$ standard deviation.

During the fouling process, the surface of the membrane was simply rinsed with deionized water at the end of the test every 1 hour and the whole process lasted for 3 hours. Permeance recovery rate and irreversible fouling rate are two important parameters for measuring anti-pollution performance during the cleaning process. The irreversible fouling rate refers to the ratio of the recovery flux after a flush to the loss flux in the first cycle. The irreversible fouling rate IRF (%) and flux recovery rate (FRR) were calculated using **eq.3** and **eq.4**

$$IRF(\%) = 1 - \frac{V_{iw} - V_s}{V_0 - V_s} \quad (3)$$

where V_{iw} represents emulsion permeances after cleaning ($L \cdot m^{-2} \cdot h^{-1} \cdot bar^{-1}$), V_s corresponds to oil-water emulsion permeances after fouling and V_0 represents the initial emulsion permeances ($L \cdot m^{-2} \cdot h^{-1} \cdot bar^{-1}$).

$$FRR(\%) = \frac{P_1}{P_0} \times 100\% \quad (4)$$

where P_1 represents the solution permeance after cleaning, P_0 means the initial emulsion permeances.

2.3 Calculation the water uptake and porosity

The water uptake ($W_{up} \text{ g} \cdot m^{-2}$), a parameter for characterizing the water absorption capacity of optimal membrane, was calculated by **eq.5**

$$W_{up} = \frac{W_{wet} - W_{dry}}{A} \quad (5)$$

where W_{up} stands for the relative increase in water quality after soaking for 24 hours in water (W_{wet}), relative to the dry membranes (W_{dry}), A is the area of the membrane.

The porosity of membrane was characterized by the weight of the ethylene glycol after wetting and the weight after drying. Porosity (ϵ) was calculated by **eq.6**

$$\varepsilon(\%) = \frac{\frac{m_1 - m_0}{\rho_1}}{\frac{m_1 - m_0}{\rho_1} + \frac{m_0}{\rho_0}} \quad (6)$$

where m_1 is the mass of the wetted membrane, m_0 is the quality of the dried membrane, ρ_1 is the density of ethylene glycol, and ρ_0 is the density of polymer.

2.4 Calculation the content of non-refrigerated water

There are different forms of hydration in membranes, including: free water, chilled water and non-refrigerable water. The non-refrigerated water is closely combined with the membrane surface, which has an important influence on the hydration capacity. Calculated by **eq.7**, **eq.8** and **eq.9**

$$W_s(\%) = \frac{m_1 - m_0}{m_1} \times 100\% \quad (7)$$

$$W_{fs}(\%) = \frac{\Delta H_s}{\Delta H_w} \times 100\% \quad (8)$$

$$W_{nfs}(\%) = W_s - W_{fs} \quad (9)$$

where m_0 is the dry weight of the membrane, m_1 is the wet weight of the membrane after soaking in water for 24 hours, and ΔH_s is the sum of the melting enthalpy in the DSC heating curve, $\Delta H_w=333.5$ (J/g). W_s is the relative water uptake of membrane. W_{fs} indicates the content of chillable water in the membrane, and W_{nfs} represents the content of non-refrigerated water in the membrane.

3. Results

3.1 ATR-FTIR spectra of membranes

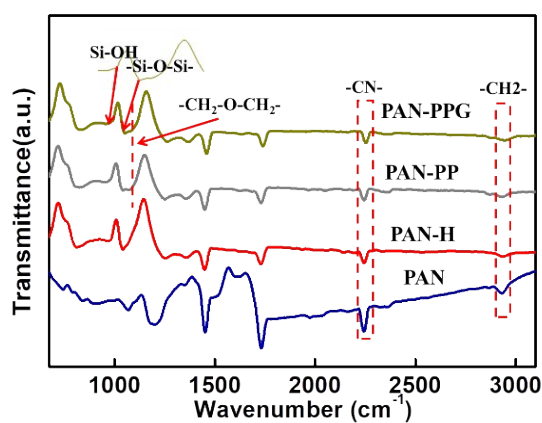


Fig. S1 ATR-FTIR spectra of the modified membranes.

The ATR-FTIR spectra can also prove the evolution of elements (**Fig. S1**). The peaks at 2246 cm⁻¹ are ascribed to -CN of PAN.^{S1} Meanwhile, the intensity of this bond decreases, because of the partial hydrolysis of -CN to -COOH.^{S2, S3} The peak at 1076 cm⁻¹ is attributed to the stretching vibration peak of CH₂-O-CH₂ derived from the PEA, PEGDGE and GPTMS. Particularly, the relatively weak peak located in 991 cm⁻¹ and 1052 cm⁻¹ are due to components of Si-OH and Si-O-Si, indicating the construction of crosslinked network structure by hydrolyzed and condensed products of GPTMS.^{S4}

3.2 The nanofiber diameter of PAN-H membrane

As shown in Fig. S2, the diameter of the PAN-H membrane is 145 ± 5 nm, indicating that the hydrolysis

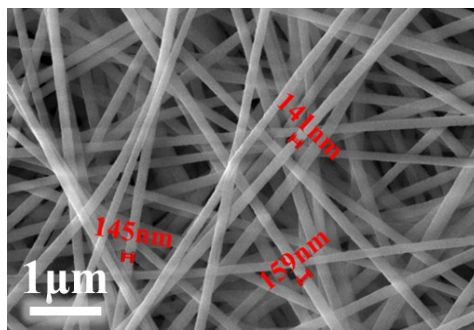


Fig. S2 SEM micrographs of PAN-H membrane

doesn't affect the diameter of the nanofiber membrane.

3.3 Morphology, hydrophilicity and emulsion permeances of membranes with different concentration

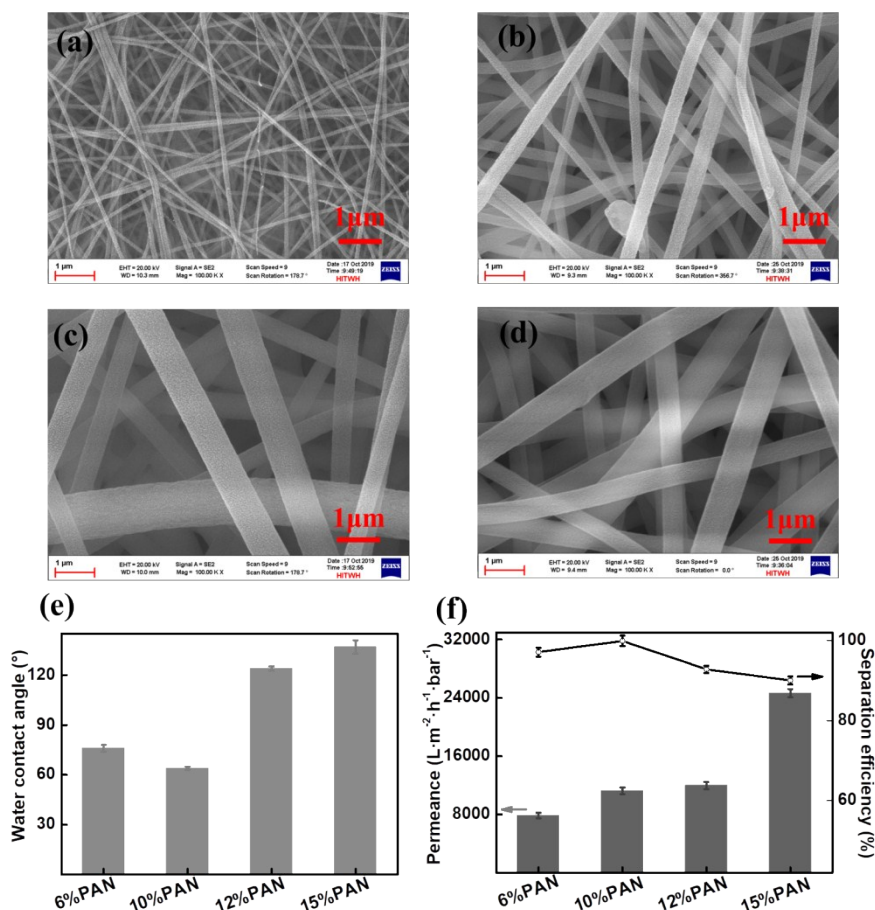


Fig. S3 Surface morphology of different concentration of membranes, including (a) 6%, (b) 10%, (c) 12% and (d) 15%. (e) The water contact angles and (f) n-octane-in-H₂O emulsion permeances of membranes.

As shown in **Fig. S3**, all membranes have smooth surfaces structure without obvious differences from the morphology of membranes. However, the nanofiber diameters change significantly. With the increasing of the concentration of the solution the diameters increase gradually, which might lead to larger pore sizes.^{S4} Therefore, the PAN membrane fabricated with 15% doping solution has the highest emulsion permeances, while the separation efficiency is lowest. It can maximize the reduction of mass transfer resistance during oil-water separation process.^{S5} From the picture of water contact angles, we can know that 10 % PAN membrane has excellent affinity with water. At the same time, 10 % PAN membrane also has excellent separation efficiency. Thence, in the process of designing membrane with asymmetric structure, 10 % PAN, 15 % PAN were used as the selective layer and supporting layer respectively.

3.4 The cross-section morphology of PAN-PPG-AS membrane

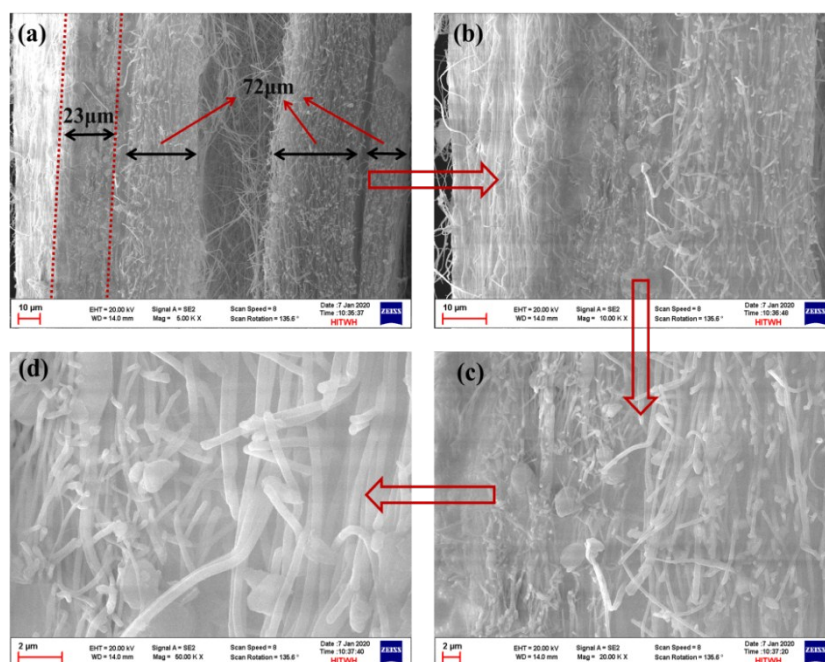


Fig. S4 The cross-sectional morphology of PAN-PPG-AS membrane at different magnifications. (a) 5.00k, (b) 10.00k, (c) 20.00k, (d) 50.00k.

From the cross-section morphology, nanofibers with different fiber diameters can be easily observed at the interface between the selective layer and the supporting layer (**Fig. S4d**). The thickness of the supporting layer and the selective layer of the well-designed nanofiber membranes are about 72 μm and 23 μm respectively. The shaded part was caused by the layered structure of the cross section during the sample preparation process for SEM testing.

3.5 Thickness and emulsion permeances of membranes with asymmetric structure

Table S1 The spinning time and thickness of membranes

Sample	PAN-PPG-AS membrane				
	Supporting layer	Selective layer			
Spinning time (h)	6	0.5	2	3	4
Thickness (μm)	68	5	21	28	39

As shown in **Table. S1**, the thickness of the selective layer and the supporting layer was measured by a micrometer, and the average of five measurements was taken. The thickness of optimal spinning time is similar to those obtained by SEM characterization in **Fig. S4**.

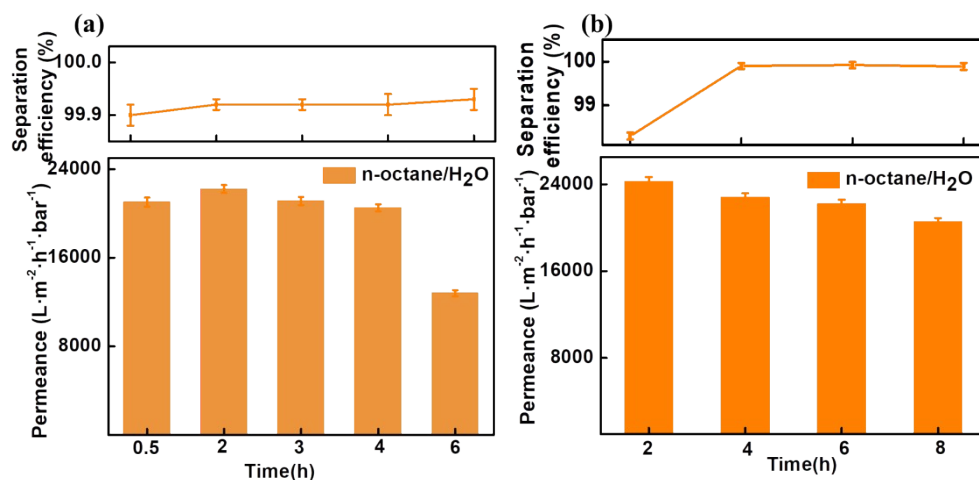


Fig. S5 The n-octane-in-H₂O emulsion permeances were measured to optimize the spinning time of (a) selective layer and (b) supporting layer.

The thickness of the selective layer and supporting layer were optimized to reduce the mass transfer resistance. And the optimal spinning time, which is positively associated with the thickness of the nanofiber membranes (**Table. S1**), was determined by examining the emulsion permeances of different membranes. In fact, the thickness of the selective layer has greatly impacted on the separation performance of the nanofiber membranes. To achieve at high permeance and rejection performance simultaneously, we designed asymmetric membrane structures compared with the symmetric nanofiber membranes. Notably, when the spinning time is less than 4 hours, the permeance of the membranes declined slightly. The membrane with 21 μm selective layer (spinning time 2 hours) shows highest permeance (22206 $\text{L}\cdot\text{m}^{-2}\cdot\text{h}^{-1}\cdot\text{bar}^{-1}$) with excellent separation efficiency (99.2 %). When the spinning time is longer than 4 hours, the mass transfer resistance increases significantly and the permeance of the membranes decreases by 37.6 % (**Fig. S5a**). Moreover, we also investigated the effects of the spinning time of supporting layer on the separation performance when the spinning time selective layer is kept at 2 hours. Notably, if the spinning time of supporting layer is 2 hours, the separation efficiency of the membranes is less than 98.3 %, which might be due to the poor strength since the thickness of the whole membranes is thinnest. With the spinning time increasing to 4~6 hours, the permeance and separation efficiency of the membranes almost keep constant. This might be due to that the permeance of the membranes is mainly dependent on the mass transfer resistance of selective layer. When the spinning time of the supporting layer increases further, the mass transfer resistance of the supporting layer increases and could not be ignored (**Fig. S5b**). Taken together, to achieve at optimum separation performance, the spinning time of the selective layer is kept at 2 hours and that of the supporting layer is chosen at 6 hours.

3.6 3D images of PAN-H membrane

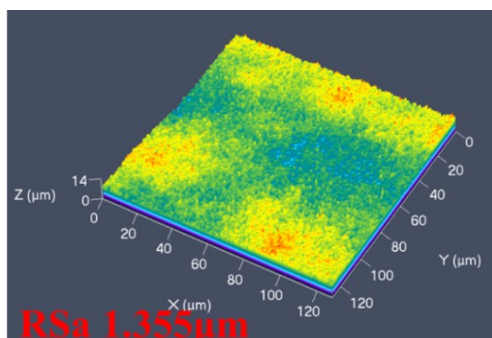


Fig. S6 3D images of Confocal laser scanning microscope about PAN-H membrane.

As shown in **Fig. S6**, The RSa value of PAN-H membranes is 1.355 μm , which is the same as the pristine PAN membranes. This indicates that hydrolysis cannot increase the roughness of the membrane surface, which is also consistent with changes in nanofiber diameters.

3.7 The pore size distribution of PAN-PPG-AS membrane

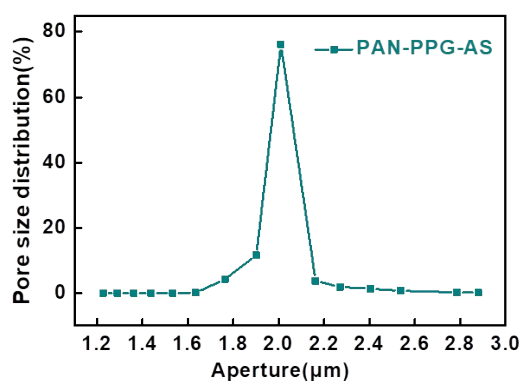


Fig. S7 The mean effective pore size of PAN-PPG-AS membrane.

The mean effective pore size of PAN-PPG-AS membranes is 2.0 μm in **Fig. S7**. As explained experimental methods, high concentration solutions will produce coarser fiber diameters in the supporting layer during electrospinning. At the same time, the nanofiber diameters directly affect the mean pore size of the membranes.^{S6} Therefore, PAN-PPG-AS membranes will get larger mean pore size, due to the supporting layer.

3.8 Water contact angles characterization of various membranes

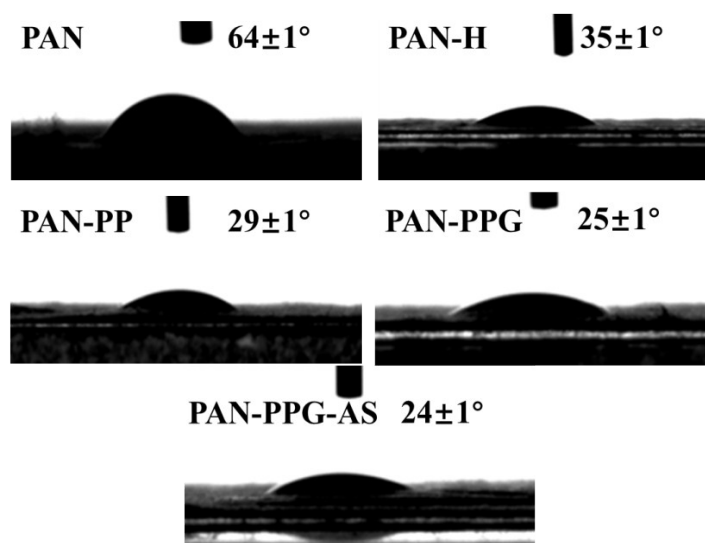


Fig. S8 Photographs of the water droplet on PAN, PAN-H, PAN-PP, PAN-PPG and PAN-PPG-AS membranes in air.

As shown in **Fig. S8**, the initial contact angles of PAN, PAN-H, PAN-PP, PAN-PPG and PAN-PPG-AS membranes reach 64.6°, 35.6°, 30.5°, 25.7° and 25.5°, and they reach 0° in 3.5s, 1.6s, 0.9s, 0.8s and 0.3s respectively.

3.9 The DSC heating curve of all membranes

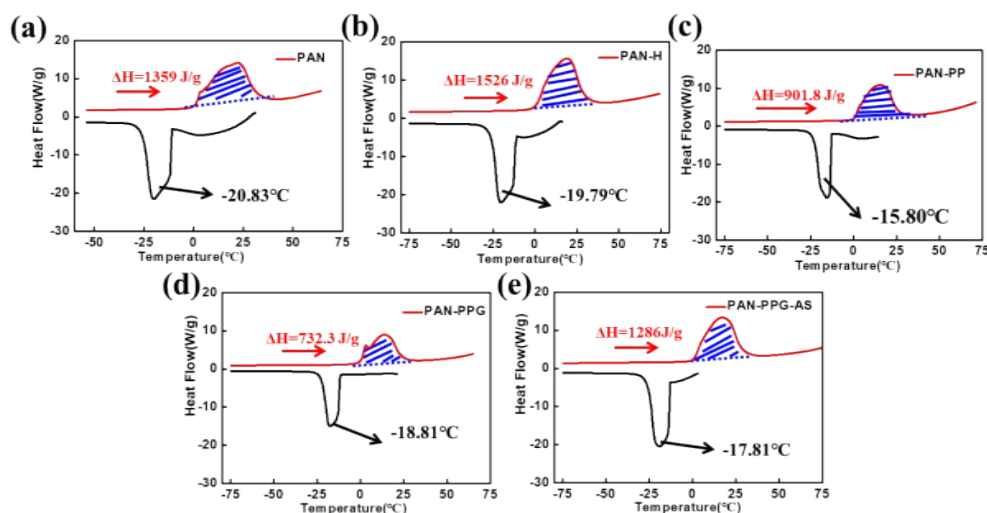


Fig. S9 DSC heating curve and crystallization peak change of (a) PAN, (b) PAN-H, (c) PAN-PP, (d) PAN-PPG, (e) PAN-PPG-AS membranes.

As shown in **Fig. S9**, the crystallization peak and the melting enthalpy of all membranes have changed, indicating that the hydration capacity variations of PAN membranes after introducing the crosslinked-structure.

3.10 The optical microscopy characterization of emulsion

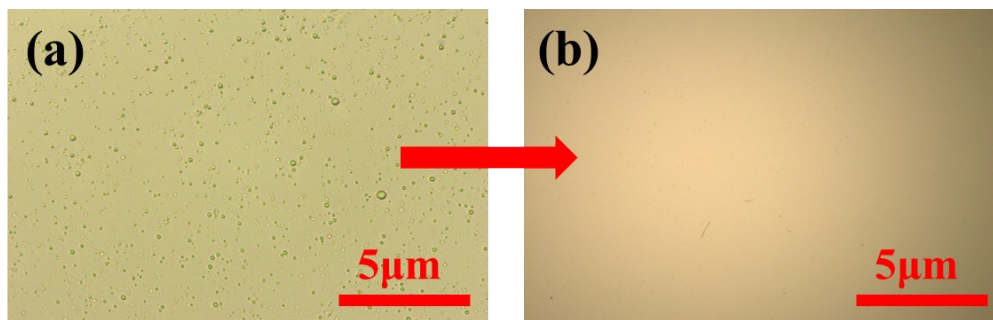


Fig. S10 The polarized optical microscopy photographs of (a) toluene-in-H₂O emulsion and (b) the filter solution.

As shown in **Fig. S10**, after PAN-PPG-AS membrane separation, the oil droplet is hardly observed by the optical microscope in the permeate solution, indicating that the PAN-PPG-AS membrane has excellent separation efficiency.

3.11 Diesel-in-H₂O emulsion permeance and separation efficiency

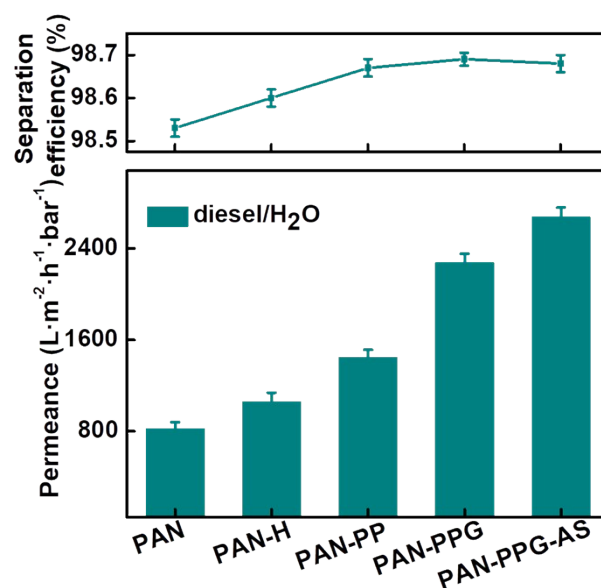


Fig. S11 Emulsion permeances and separation efficiency of all kinds of PAN-based membranes for diesel-in-H₂O emulsion

As shown in **Fig. S11**, the diesel oil removal rates of various PAN based nanofiber membranes fluctuated around 98.6%, and the separation efficiency of PAN-PPG-AS membrane can reach 98.68 %. After the introduction of the crosslinked network and the asymmetric structure, the diesel-in-H₂O emulsion permeance of PAN-PPG-AS membrane reaches 2674 L·m⁻²·h⁻¹·bar⁻¹, which increases by 325 % compared with that of the pristine PAN membrane. Similarly, the PAN-PPG-AS membranes exhibited highest permeance and rejections because of its excellent pore structure and hydrophilicity. The permeance towards the diesel in water emulsion is much lower than that of n-octane-in-H₂O emulsion because of its higher intrinsic viscosity and complex composition of the diesel solution.

3.12 Nanoparticle size of emulsion and filtration

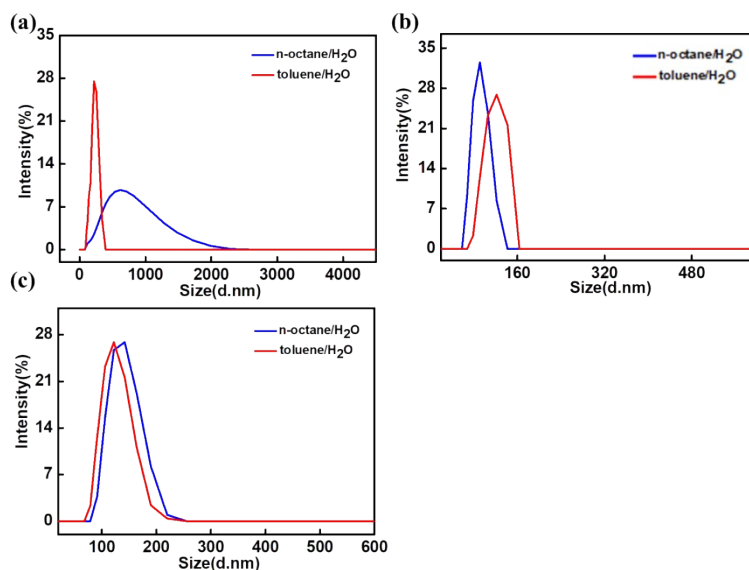


Fig. S12 (a) Particle size of n-octane-in-H₂O emulsion and toluene-in-H₂O emulsion. (b) The particle size of filtration by PAN-PPG-AS membrane. (c) The particle size of filtration by PAN membrane.

The size of the n-octane emulsion (68 nm-2300 nm) and the toluene emulsion (78 nm-342 nm) are characterized in **Fig. S12a**. Filtration droplets of (c) PAN are basically kept in the range of 91 nm-220 nm (N/E), 78 nm-220 nm (T/E). However, the filtration droplets of (b) PAN-PPG-AS membrane is kept in a smaller scale including 68 nm-122 nm (N/E) and 78 nm-142 nm (T/E).

Notes and references

- S1. Y. Xu, D. Guo, T. Li, Y. Xiao, L. Shen, R. Li, Y. Jiao and H. Lin, *J. Colloid. Interf. Sci.*, 2020, **565**, 23-34.
- S2. S. Munirasu, F. Banat, A. A. Durrani and M. A. Haija, *Desalination*, 2017, **417**, 77-86.
- S3. X. Yang, L. Yan, F. Ran, Y. Huang, D. Pan, Y. Bai and L. Shao, *J. Membr. Sci.*, 2020, **597**, 117753.
- S4. Z. Wang, X. Jiang, X. Cheng, C. H. Lau and L. Shao, *ACS Appl. Mater. Interface*, 2015, **7**, 9534-9545.
- S5. J. Cao, Y. Su, Y. Liu, J. Guan, M. He, R. Zhang and Z. Jiang, *J. Membr. Sci.*, 2018, **566**, 268-277.
- S6. X. Zhao, N. Jia, L. Cheng, L. Liu and C. Gao, *J. Membr. Sci.*, 2018, **560**, 47-57.
- S7. M. Tao, L. Xue, F. Liu and L. Jiang, *Adv. Mater.*, 2014, **26**, 2943-2948.
- S8. Z. Xiong, H. Lin, Y. Zhong, Y. Qin, T. Li and F. Liu, *J. Mater. Chem. A*, 2017, **5**, 6538-6545.
- S9. Q. Zhang, N. Liu, Y. Wei and L. Feng, *Soft. Matter.*, 2018, **14**, 2649-2654.
- S10. J. Zhang, Z. Wang, Q. Wang, J. Ma, J. Cao, W. Hu and Z. Wu, *J. Membr. Sci.*, 2017, **537**, 263-271.
- S11. Y. Chen, Q. Li, X. Chen and X. Xu, *New J Chem.*, 2019, **43**, 9696-9705.
- S12. J.-X. Wu, J. Zhang, Y.-L. Kang, G. Wu, S.-C. Chen and Y.-Z. Wang, *ACS Sustain. Chem. Eng.*, 2017, **6**, 1753-1762.
- S13. Y. Zhang, Y. Chen, L. Hou, F. Guo, J. Liu, S. Qiu, Y. Xu, N. Wang and Y. Zhao, *J. Mater. Chem. A*, 2017, **5**, 16134-16138.
- S14. J. Feng, M. Sun and Y. Ye, *J. Mater. Chem. A*, 2017, **5**, 14990-14995.
- S15. J. Wang and H. Wang, *Sep. Purif. Technol.*, 2018, **195**, 358-366.

- S16. F.-N. Meng, M.-Q. Zhang, K. Ding, T. Zhang and Y.-K. Gong, *J. Mater. Chem. A*, 2018, **6**, 3231-3241.
- S17. T. Huang, L. Zhang, H. Chen and C. Gao, *J. Mater. Chem. A*, 2015, **3**, 19517-19524.
- S18. L. Zhang, L. Cheng, H. Wu, T. Yoshioka and H. Matsuyama, *J. Mater. Chem. A*, 2018, **6**, 24641-24650.
- S19. S. J. Gao, Z. Shi, W. B. Zhang, F. Zhang, and J. Jin, *ACS Nano*, 2014, **6**, 6344-6352.
- S20. H. Shi, Y. He, Y. Pan, H. Di, G. Zeng, L. Zhang and C. Zhang, *J. Membr. Sci.*, 2016, **506**, 60-70.
- S21. Y. Zhu, J. Wang, F. Zhang, S. Gao, A. Wang, W. Fang and J. Jin, *Adv. Funct. Mater.*, 2018, **28**, 1801944.
- S22. F. Zhang, W. B. Zhang, Z. Shi, D. Wang, J. Jin and L. Jiang, *Adv. Mater.*, 2013, **25**, 4192-4198.